1   **The mobility of Nb in rutile-saturated NaCl- and NaF-bearing aqueous fluids from 1-6.5**
2   **GPa and 300-800 °C**

3   ELIZABETH A. TANIS[1,2], ADAM SIMON[1], OLIVER TSCHAUNER[2,3], PAUL CHOW[4], YUMING XIAO[4],
4   PAMELA BURNLEY[2,3], CHRISTOPHER J. CLINE II[2,3], JOHN M. HANCHAR[5], THOMAS PETTKE[6], GUOYIN
5   SHEN[5], YUSHENG ZHAO[5]

6   [1]Earth & Environmental Sciences, University of Michigan
7   [2]High Pressure Science and Engineering Center, University of Nevada, Las Vegas
8   [3]Department of Geoscience, University of Nevada, Las Vegas
9   [4]HPCAT, Carnegie Institute of Washington, Argonne IL
10   [5]Earth Sciences, Memorial University of Newfoundland
11   [6]Institute of Geological Sciences, Bern, Switzerland

12   **ABSTRACT**

13   Rutile (TiO_2) is an important host phase for high field strength elements (HFSE) such as Nb in

14   metamorphic and subduction zone environments. The observed depletion of Nb in arc rocks is

15   often explained by the hypothesis that rutile sequesters HFSE in the subducted slab and

16   overlying sediment, and is chemically inert with respect to aqueous fluids evolved during

17   prograde metamorphism in the forearc to subarc environment. However, field observations of

18   exhumed terranes, and experimental studies, indicate that HFSE may be soluble in complex

19   aqueous fluids at high pressure (i.e., > 0.5 GPa) and moderate to high temperature (i.e., > 300

20   °C). In this study, we investigated experimentally the mobility of Nb in NaCl- and NaF-bearing

21   aqueous fluids in equilibrium with Nb-bearing rutile at pressure-temperature conditions

22   applicable to fluid evolution in arc environments. Niobium concentrations in aqueous fluid at

23   rutile saturation were measured directly by using a hydrothermal diamond anvil cell (HDAC)

24   and synchrotron x-ray fluorescence (SXRF) at 2.1 to 6.5 GPa and 300-500 °C, and indirectly by

25   performing mass loss experiments in a piston-cylinder (PC) apparatus at ~1 GPa and 700-800

26   °C. The concentration of Nb in a 10 wt% NaCl aqueous fluid increases from 6 to 11 μg g^{-1} as

27   temperature increases from 300 to 500 °C, over a pressure range from 2.1 to 2.8 GPa, consistent

28   with a positive temperature dependence. The concentration of Nb in a 20 wt% NaCl aqueous

29   fluid varies from 55 to 150 μg g^{-1} at 300 to 500 °C, over a pressure range from 1.8 to 6.4 GPa;

30   however, there is no discernible temperature or pressure dependence. The Nb concentration in a

31   4 wt% NaF-bearing aqueous fluid increases from 180 to 910 μg g^{-1} as temperature increases from

32   300 to 500 °C over the pressure range 2.1 to 6.5 GPa. The data for the F-bearing fluid indicate

33   that the Nb content of the fluid exhibits a dependence on temperature between 300 and 500 °C at

34   ≥2 GPa, but there is no observed dependence on pressure. Together, the data demonstrate that the

35   hydrothermal mobility of Nb is strongly controlled by the composition of the fluid, consistent

36   with published data for Ti. At all experimental conditions, however, the concentration of Nb in

37   the fluid is always lower than coexisting rutile, consistent with a role for rutile in moderating the

38   Nb budget of arc rocks.

39   **INTRODUCTION**

40   Arc magmas bear a characteristic geochemical trace element signature consisting of a

41   depletion of high field strength elements (HFSE) and enrichment in large ion lithophile elements

42   (LILE) and light rare earth elements (LREE) relative to mid-ocean ridge basalts (Gill, 1981;

43   Hawkesworth et al., 1991). Three working hypotheses have been developed to explain the

44   geochemical signature of arc magmas. The *first* hypothesis is that ascending aqueous fluids from

45   the slab are enriched in LILE and LREE, relative to HFSE, and thus transfer this signature to

46   partial melts produced in the mantle. This hypothesis suggests that mineral phases (e.g.,

47   clinopyroxene) in the mantle control the HFSE budget of mantle-derived silicate melt

48   (Hawkesworth, 1993a,b; Kelemen et al., 1990; Foley et al., 2000, Audétat and Keppler, 2005).

49   The *second* hypothesis is that melt extraction from the mantle at a back-arc spreading center

50   depletes the mantle in HFSE prior to its interaction with slab-derived fluid at the base of the arc

51   volcano plumbing system (McCulloch and Gamble, 1991; Woodhead et al., 1993). This

52   hypothesis requires the mantle wedge to be re-fertilized by fluids during melt extraction. The

53   downward motion of the subducted slab drags this depleted mantle material into the mantle

54   wedge above the slab, yielding a strong depletion of HFSE during subsequent partial melting of

55   the depleted mantle.

56   The *third* and most widely accepted hypothesis is that specific minerals in the subducted slab

57   retain the HFSE during slab dehydration; for example, rutile moderates Nb and Ta, and zircon

58   moderates Zr and Hf partitioning of the fluids that may ascend into the mantle (Saunders et al.,

59   1980; Green, 1981; Brophy and Marsh, 1986; Ryerson and Watson, 1987; Morris et al., 1990).

60   The resulting trace element abundance patterns are preserved in arc magma owing to the very

61   low abundances of the HFSE in the mantle and slab-evolved fluid. Experimental studies of rutile

62   solubility in pure H_2O support this hypothesis (Audétat and Keppler, 2005; Tropper and

63   Manning, 2005). However, Manning (2004) emphasized that slab-derived fluids are not pure

64   H_2O, but rather contain significant amounts (i.e., up to and exceeding 10 wt% dissolved solutes)

65   of alkalis (Na, K), halogens (Cl, F) and aluminosilicate components (i.e., Si, Al). Experimental

66   data generated at 0.5-2 GPa and 700-1100 °C demonstrate that the addition of these solutes to

67   aqueous fluid increases the solubility of pure rutile in the fluid by several orders of magnitude

68   relative to pure water (Audétat and Keppler, 2005; Antignano and Manning, 2008; Manning et

69   al., 2008; Rapp et al., 2010; Hayden and Manning, 2011). For example, at 800 °C and 1 GPa, the

70   solubility of pure rutile in aqueous fluid increases from 18 ± 5 μg g^{-1} Ti in pure water to 152 ± 5

71   μg g^{-1} Ti in aqueous fluid that contains 3.162 – 2.423 wt% dissolved silicate (Antignano and

72   Manning, 2008). Rapp et al. (2010) reported that at 800 °C and 0.5 GPa, the solubility of pure

73   rutile in aqueous fluid increased from 212 ± 18 μg g^{-1} Ti in pure water to 11,912 μg g^{-1} Ti in fluid

74   that contains 10 wt% dissolved NaF. These experimental data evince that the solubility of pure

3

75   rutile in aqueous fluid varies with fluid chemistry. However, existing experimental data do not

76   overlap with the pressure-temperature paths for subduction zones (Figure 1; Hacker, 2008) and

77   require extrapolation when applied to the conditions of fluid evolution during prograde

78   metamorphic devolatilization, which begins in the forearc at temperatures as low as 300 °C (cf.

79   Bebout et al., 1999; Hacker, 2008). Notably, all of the aforementioned studies used the solubility

80   of pure rutile in aqueous fluid as a proxy to predict the fluid mobility of all HFSE. It has been

81   shown that this may be appropriate for Zr (Kelemen et al., 1990). However, Jenner et al. (1994)

82   reported much higher rutile / tonalite melt partition coefficients for Nb ($D_{Nb}^{rutile/fluid}$ = 52.6) and Ta

83   ($D_{Ta}^{rutile/fluid}$ = 99.5) than for Zr ($D_{Zr}^{rutile/fluid}$ = 4.76), indicating the potential error of inferring the

84   mobility of Nb and Ta based on Ti.

85   The enhanced fluid compatibility of Ti in complex aqueous solutions suggests that Nb may

86   be dissolved and transported in such fluids. There is an absence of data that constrain the

87   mobility of HFSE such as Nb in aqueous fluid. Brenan et al. (1994) and Stalder et al. (1998)

88   experimentally investigated the partitioning of Nb between rutile and aqueous fluid at 1-5 GPa

89   and 900-1100 °C. These pressures overlap with those in the forearc to subarc region, but the

90   temperatures are higher by several hundred degrees then those obtained during subduction

91   (Figure 1). The experimental assemblage of Stalder et al. (1998) contained only pure H_2O,

92   whereas Brenan et al. (1994) added 3 wt% SiO_2, in addition to HCl, NaCl and Al, to the fluid in

93   three separate experiments. Brenan et al. (1994) reported that the addition of NaCl, HCl and Al

94   to the fluid-rutile assemblage affected the value of $D_{Nb}^{rutile/fluid}$. For example, at 900 °C and 1 GPa,

95   the value of $D_{Nb}^{rutile/fluid}$ (± 1σ) was 193 ± 44 for water with 3 wt% SiO_2, and increased to 217 ± 72

96   with the addition of 1m HCl-fluid; 325 ± 107 with the addition of 1m NaCl-fluid; and 484 ± 140

97   for fluid that contained 300 μg g^{-1} Al. Similar results were reported for Ta (Brenan et al., 1994).

4

98   These results indicate that the compatibility of HFSE in pure H_2O and dilute aqueous fluid in

99   equilibrium with rutile is generally quite low, and that the partitioning of HFSE from rutile to

100   aqueous fluid actually decreases with increasing complexity of the aqueous fluid. However, this

101   latter finding is not consistent with the solubility data for pure rutile in complex aqueous fluids as

102   mentioned above (Audétat and Keppler, 2005; Antignano and Manning, 2008; Manning et al.,

103   2008; Rapp et al., 2010; Hayden and Manning, 2011).

104   To quantitatively evaluate the fluid mobility of HFSE in light of the more recent

105   experimental studies mentioned above that support a strong role of fluid chemistry in dissolving

106   rutile (i.e., up to 1 wt% Ti in the fluid), and presumably other HFSE, there is the critical need to

107   assess experimentally the effects of prograde metamorphic devolatilization and the relationship

108   between fluid chemistry and trace element mobility at pressures and temperatures where fluids

109   evolve during subduction (Figure 1). In this study, new experimental data are presented that

110   quantify the mobility of Nb in rutile-saturated NaCl- and NaF-bearing aqueous fluids at 1 to 6.5

111   GPa and temperatures of 300 to 800 °C, pressure and temperature conditions appropriate for

112   prograde devolatilization paths in cold to hot subduction zones (Figure 1).

                              EXPERIMENTAL METHODS

Rutile Synthesis and Characterization

115   The synthetic Nb-doped rutile (Nb-TiO_2) crystals used in this study were prepared following

116   the method described in Hanchar et al. (2001). High-purity TiO_2 and Nb_2O_5 were weighed to

117   achieve 6 mol% TiO_2 and 0.09 mol% Nb_2O_5, then mixed in an HNO_3-cleaned agate mortar and

118   pestle under absolute ethanol and allowed to dry. Once dried, the powders were mixed under

119   absolute ethanol with the fluxing agents Li_2MoO_4 and MoO_3 in the following proportions: 84

120   mol% MoO_3 and 10 mol% Li_2MoO_4; and the remaining TiO_2 - Nb_2O_5 mixture, mentioned above,

5

121   then allowed to dry. The mixture was then transferred to an HNO_3 -cleaned Pt crucible with a

122   tightly fitted Pt lid. The crucible was lowered into the "hot spot" of a preheated (1200 °C)

123   Deltech $MoSi_2$ vertical tube furnace and held at constant temperature for seven days, permitting

124   the flux to evaporate. Using a type S control thermocouple, the temperature in the hot spot was

125   measured to be stable within ±5 °C. When rutile saturation was reached, the rutile crystals began

126   to grow in the residual flux. Upon completion of the synthesis, no residual flux remained in the

127   crucible. The crystals were removed from the Pt crucible with tweezers and cleaned in

128   concentrated HNO_3. Powder x-ray diffraction was done to ensure that the rutile structure was

129   obtained and not the TiO_2 polymorphs brookite or anatase.

130   The concentrations of Nb, Ti and Mo in the starting rutile were quantified by using

131   wavelength dispersive spectroscopy on a Cameca SX100 electron probe microanalyzer (EPMA)

132   and laser ablation inductively coupled mass spectroscopy (LA-ICP-MS). For EMPA, a beam

133   current of 50 nA (calibration and analysis) and an accelerating voltage of 15 kV were used.

134   Counting times (30 s at the peak) yielded detection limits for Nb, Ti, and Mo of approximately

135   330, 590 and 300 $\mu g\ g^{-1}$, respectively. Standard ZAF techniques were used for the matrix

136   corrections. The standards used included pure rutile (TiO_2), Nb_2O_5, and pure Mo metal. A

137   different crystal and detector combination was used for each element: LIF for Ti; and LPET for

138   Nb and Mo. Each crystal was imaged by using back-scattered electrons (BSE), and then a EMPA

139   line traverse across the length of the sample was done to evaluate chemical homogeneity. The

140   concentrations of Nb and Mo of starting crystals were 0.95 ± 0.1 wt%, and 0.02 ± 0.03 wt%,

141   respectively; Mo is sourced form the flux used during mineral synthesis. Some crystals displayed

142   zoning in BSE images, and for these crystals an analytical line traverse from the rim to the core

143   of the crystal. The beam spot measured 5 μm and the step size for the rim to core line traverse

6

144   was 2 μm (Figure 2 a, b). All totals summed to $100 \pm 1\%$. Depth profiles of the Nb concentration

145   through starting (Figure 2c, d, Figure 3a) and piston cylinder run-product (Figure 3b) crystals

146   were also obtained by using LA-ICP-MS, by drilling perpendicular to crystal growth surfaces

147   and integrating single pulses individually. The ablation rate of a single pulse amounted to about

148    $0.10\,\mu$m depth. The LA-ICP-MS analyses were performed following the analytical method

149   outlined in Pettke (2006) and Pettke et al. (2012). The data indicate that the starting crystals

150   contain an average of 1.03 ± 0.2 wt% Nb, which is consistent with the EMPA results. The LA-

151   ICP-MS data also indicate that some starting crystals have a rim (of several μm thickness) that is

152   enriched in Nb and Mo (Figures 2c, d and 3a). For example, the LA-ICP-MS depth profile

153   shown in Figure 2d indicates that the concentration of Nb at the rim of this starting rutile crystal

154   was ~8 wt%, and decreased to ~1 wt% over a distance of $2\,\mu$m into the center of the crystal. This

155   Nb-enriched rim likely reflects either a quench-effect during synthesis, or the kinetics of Nb

156   incorporation into rutile during synthesis.

157   **SXRF experiments**

158   The HDAC (Bassett et al., 1993) used in the current study was equipped with two

159   opposing 500 or 800 μm culet diamonds. Molybdenum wires, coiled around a tungsten carbide

160   seat that supported each diamond anvil, provided resistive heating. Two K-type (NiCr-NiAl)

161   thermocouples, one on each diamond, were used to measure temperature. The HDAC was heated

162   resistively by using variable transformers that facilitated flexible heating rates and allowed us to

163   maintain temperature stability to ~5 °C. The HDAC was calibrated up to 800 °C by observing

164   the melting point or phase transition temperature of $NaNO_3$, CsCl, and NaCl, and measured

165   temperatures were systematically lower by ~0.85% relative to the actual melting point or phase

166   transition (Kerrigan, 2011). A 1% H_2-Ar gas mixture flowed constantly through the HDAC

7

167   during the measurements to prevent corrosion of the diamonds and the heaters.

168   A gold-lined rhenium gasket was pre-indented to a thickness of ~120 μm and a hole of

169   200 μm or 400 μm diameter was drilled for 500 and 800 μm diamond culets, respectively. A Nb-

170   rutile crystal, measuring approximately 40x40x20 μm by using a optical microscope, was loaded

171   into the sample chamber. Fluids were prepared by adding known masses of NaCl and NaF to

172   deionized, lab grade water in calibrated volumetric flasks to make either 10 wt% NaCl, 20 wt%

173   NaCl or 4 wt% NaF aqueous solution. The fluid was then added by using a micro syringe and the

174   HDAC was immediately sealed and pressurized to ~0.5 GPa. There was no evaporation during

175   loading and no observed halite precipitation during any of the experiment runs; hence, the

176   salinity of the added fluid represents that added to the cell. Further, as described below, an on-

177   line microscope was used to make visual observations of the experimental sample chamber

178   during runs, and the presence of a salt crystal was never detected. The phase assemblage, based

179   on visual observation, consisted only of fluid and rutile crystal. Thus, we are confident that the

180   salinity of the fluid at all pressure-temperature conditions was equal to the salinity of the fluid

181   added to the sample chamber.

182   The SXRF experiments were done at undulator beamline 16-IDD (HPCAT) at the

183   Advanced Photon Source (APS) synchrotron facility at Argonne National Laboratory. The

184   incident beam energy was 27 keV. The beam was focused to a spot size of 35x50 μm full-width

185   at half maximum (FWHM) by using a pair of Kirkpatrick-Baez mirrors. A 100 μm round pinhole

186   was used before the HDAC to reduce the tails of the incident beam, which contained a flux of

187   1.14×10^{12} photons/s. The incident beam was projected into the sample chamber through the

188   diamonds of the HDAC. The fluorescence from the sample was collected in a 170°

189   backscattering geometry by using a Vortex-EX silicon drift detector that was positioned ~0.8 m

8

190   from the sample. To reduce the background, a pair of large collimating slits were placed before

191   the detector. The energy channels of the multi-channel analyzer were calibrated with ^{55}Fe, ^{57}Co,

192   and ^{109}Cd radioactive sources. The position and aperture of the detector was optimized by using

193   the SXRF peak for pure Nb metal. There was no Nb contamination from any component of the

194   HDAC, which was confirmed by SXRF analyses of an empty cell.

195   SXRF spectra of the empty HDAC (0 μg g^{-1} Nb) and the same HDAC containing

196   standard solutions of 300, and 1000 μg g^{-1} Nb were collected before each experimental run and

197   used to build a calibration curve to determine the Nb concentration of experimental fluids,

198   similar to the process described in Tanis et al. (2012) and shown in Figure 5. The Nb-rutile

199   crystal position was found visually by using an online optical microscope and confirmed by

200   SXRF. The beam was then positioned ≥50 μm away from the crystal and the HDAC was rotated

201   5° to ensure no signal contamination from the crystal. The HDAC was heated from room

202   temperature to 300 °C, and the pressure inside the sample chamber was determined by using

203   XRD patterns from the Au gasket liner. The XRD data were collected by using a MAR 165

204   CCD detector placed in the forward scattering direction, and pressure was monitored throughout

205   the run by collecting XRD patterns from the Au gasket liner. The variation of the Au lattice

206   parameters change with pressure and, thus, act as an internal pressure standard. The XRD

207   patterns showed no evidence of grain growth and displayed well-defined Debye rings at all

208   temperatures. The XRD patterns were integrated and corrected for geometric distortions by using

209   Fit2D (Hammersley, 1997). A NIST standard CeO$_2$ pattern was collected and used for the XRD

210   calibration. Gold pressure was determined by using the method of Dorogokupets and Dewaele

211   (2007). The diamonds used in the cell assembly did not contain any modifications, such as a

212   recess for SXRF collection (e.g. Schmidt and Rickers, 2003) which allowed measurements to be

213   made at pressures higher than published studies in the HDAC and to collect SXRF data in a 170°

214   backscattering geometry.

215   Fluorescence spectra for Nb were collected iteratively in 300 s intervals. Steady state was

216   assessed by evaluating the time-dependence of the fluorescence signal. Once the Nb peak, at a

217   unique pressure and temperature condition, became time-invariant, it was interpreted to reflect

218   the attainment of steady-state conditions. This took approximately 30–40 minutes at each unique

219   pressure-temperature point. The time to reach steady state is consistent with observations

220   reported by Sanchez-Valle et al. (2003), Schmidt et al. (2007), Manning et al. (2008), and Louvel

221   et al. (2014). Once steady-state conditions were achieved, spectra were collected in 300 s

222   intervals for ∼3 h. The temperature was then increased to 400 °C, and subsequently to 500 °C,

223   and the data collection procedure was repeated at each temperature (Figure 6). Steady state

224   conditions were further assessed after the experiment by looking at the integrated spectra for

225   each time step. Only experiments that contained an average standard deviation over the entire

226   time range of less then 15% were considered; afterwards, a fit of the data was made to ensure

227   that the R^2 value was <0.1, essentially time invariant. For example, in Figure 6, the integrated,

228   unnormalized, raw data as a function of time for Runs 20110804 (top) and 20110805 (bottom)

229   are shown. During Run 20110804, at 300 °C there were large variations (average standard

230   deviation >12%) in the signal, due to major beam fluctuations, therefore only 300°C data in the

231   later time frame (where R^2 of the fit <0.02) was used.

232   The experimental run conditions and results are reported in Table 1. Increasing the

233   temperature of the HDAC results in a change in the pressure of the sample chamber, owing to

234   relaxation of the Re-Au gasket. Pressure at each run temperature was quantified by using XRD

235   patterns of Au as previously described, which allowed us to monitor changes in pressure before

10

236   and after each sequence of fluorescence data were collected. The reported pressure is the average

237   of starting and final pressure. The fluorescence spectra from the standard solutions (Figure 5)

238   and high P-T experiments were separately summed, and normalized to the intensity of the

239   incoming beam. Peak intensities were corrected for absorption in the by fluid using the fluid

240   composition and density, following the procedure described in Sanchez-Valle et al. (2003),

241   Schmidt et al. (2007), Manning et al. (2008), and Louvel et al. (2014). A linear background was

242   subtracted and the area of the Nb fluorescence peak was fit and integrated by using the program

243   Fityk (Wojdyr, 2010). The integrated peak area was then normalized to time (Tanis et al., 2012).

244   The density of the aqueous fluid was calculated after the experiment based on the experimental

245   pressure and temperature of the run conditions by using the EOS of NaCl-H_2O fluids from

246   Mantegazzi et al. (2013). There are no published EOS data for NaF-bearing aqueous fluid;

247   hence, the EOS of a 4 wt% NaCl- H_2O fluid was used as a proxy for the NaF-bearing aqueous

248   fluid. Uncertainties for the Nb concentration of the fluids measured in the SXRF experiments at

249   high pressures and temperatures were calculated based on the fitting errors of the summed

250   spectra, and also include propagating the fitting errors from the standard calibration.

251   The iterative nature of the SXRF experimental technique (i.e., loading one fluid-crystal

252   assemblage and collecting fluorescence data at multiple P-T points during a single run)

253   combined with the small size of the loaded crystal, prevented recovering and analyzing the rutile

254   crystal from each unique P-T condition. Thus, partition coefficients for Nb between fluid and

255   rutile were not determined. The experimentally determined diffusion coefficient of Nb in rutile

256   ranges from $D = 5.6 \times 10^{-19}$ to 3×10^{-21} m^2/s at 800°C (Sheppard et al., 2007; Marschall et al.,

257   2013), and extrapolation indicates that Nb is effectively immobile in rutile at the experimental

258   conditions of this study. Over the timescales of the experiments (t<10 hrs) the diffusion distance

11

259   would be less then 0.14 μm. Therefore, it can be assumed that the Nb:Ti ratio of the rutile did not

260   change during the experiments, and that the Nb concentration of the fluid is controlled by rutile

261   solubility. However, the presence of Nb-enriched rims on rutile crystals disallowed the use of

262   Nb/Ti ratios of the starting crystals in order to use the measured Nb content of the fluid to

263   calculate apparent Ti values of the fluid. The data reported in the present study for the

264   concentration of Nb in NaCl- and NaF-aqueous fluids demonstrate the strong effect of dissolved

265   halogens on increasing the Nb concentration of aqueous fluid.

266   **SXRF Mapping**

267   For experimental run 20130205 (4 wt% NaF, 300-600 °C, 2.13-3.07 GPa), data were

268   collected by using a SXRF mapping technique. The cell was positioned in direct line of the

269   detector (versus angled to hide the crystal signal) to maximize Nb count rate. The position of the

270   HDAC was moved in steps of 25 μm in the x (horizontal) and y (vertical) directions and SXRF

271   spectra were taken at each x-y position, as well as, the values of the incoming and out going

272   beam intensity. Figures 6a and b demonstrate how the sample chamber was mapped in 2-D (x

273   and y position, where the color scale is beam intensity) and in 3-D (x and y position, where the z-

274   axis and color scale are intensity), respectively. Figures 6c and d are similar 2-D and 3-D figures

275   that show how the spatial position of the Nb-rutile crystal was constrained. The concentration of

276   Nb in the fluid was determined by summing and integrating the normalized spectra, significantly

277   away (50-75 μm) from the Nb-rutile crystal spectra. A SXRF map of the HDAC containing 300

278   and 600 μg g^{-1} Nb standard were also collected for calibration.

279   **Piston Cylinder Mass Loss Experiments**

280   The mass loss experiments were done in a Griggs-type modified piston-cylinder

281   apparatus. Piston cylinder run conditions and results are provided in Table 2. Temperature

12

282   gradients were modeled by using the "CellAssembly" thermal modeling program (Hernlund et

283   al., 2006), and confirmed by using two thermocouples placed on each side of the capsule. The

284   temperature gradient was a maximum of 5 °C across all dimensions (~7 mm long, 5 mm outer

285   diameter) of the capsule. Confining pressure on the sample was derived from the oil pressure in

286   the piston cylinder ram, which was measured with an Omegadyne pressure transducer. The

287   nominal sample pressure was calculated by dividing the load exerted by the ram by the area of

288   the confining pressure piston. The nominal sample pressure can deviate from the actual pressure

289   by up to 10% owing to frictional effects (Bose and Ganguly, 1995; Burnley and Getting, 2012),

290   which are more pronounced at low pressure. The experimental charges each contained a single

291   crystal of Nb-rutile and 30 μg fluid in a platinum capsule. The capsule design was made by

292   cutting a ~7 mm length piece of Pt tubing and welding a circular disk "lid" onto the bottom and

293   top (after the crystal and fluid were loaded). The capsule was weighed before and after welding

294   to ensure no fluid was lost. The starting crystal was weighed 4 times by using a Mettler XP26

295   DeltaRange balance, and the values averaged for accuracy, before being loaded into the capsule.

296   The hot piston-in technique of Manning and Boettcher (1994) was used to cold compress to ~50

297   MPa and then heating and compressing in alternating increments to minimize compression and

298   expansion of the capsule relative to other sample assembly parts. Conditions were maintained for

299   ≥8 hours once the desired pressure and temperature were attained. The sample was quenched by

300   shutting off power to the apparatus, which results in a temperature drop to <30 °C in <30 s. This

301   minimizes, if not eliminates, back-reaction between the crystal and fluid during quench

302   (Antignano and Manning, 2008). After quench, the capsule was cleaned and weighed, then

303   punctured and dried at 120 °C for 1 hour. The capsule was weighed again, opened, and the

304   crystal was removed. Comparison of the total capsule weight before and after the experiments

13

305   showed no fluid was lost during the experiment. The crystal was cleaned with isopropanol,

306   weighed 4 times, and then averaged to determine the mass loss during the experiment.

307   Piston cylinder run products included the partially dissolved starting crystal and fine-

308   grained quench "roe" crystals (ca. 20 μm diameter, run 20130522), consistent with crystals that

309   formed during quench (cf. Antignano and Manning, 2008). In experiment 20130527, broken

310   crystal fragments (ca. 0.5 mm) were recovered along with the primary crystal. Final

311   concentrations of Nb and Mo of rutile crystals recovered from the mass-loss experiments were

312   determined by using EMPA and LA-ICP-MS, as previously described (Table 2). The EMPA and

313   LA-ICP-MS (Figure 3b) results demonstrate that run-product crystals were homogeneous with

314   respect to Nb and Ti, and contained no detectable Mo. Uncertainties for Nb concentrations in the

315   fluid from the mass loss experiments reflect propagation of weighing errors, the analytical error

316   from the EMPA and LA-ICP-MS analysis, as well as consideration of the thin Nb-enriched rim

317   on the starting rutile crystal. To account for the starting crystal containing a Nb-enriched rim, a

318   minimum value of mass loss was calculated by using the final (bulk) Nb concentration of the

319   recovered rutile crystal from each experiment, determined by using LA-ICP-MS, and a

320   maximum value assuming 8 wt% Nb (Table 2). For example, in experiment 20130314 the mass

321   loss is 24 μg. If a spherical crystal is assumed, this corresponds to a radius difference of ~5 μm,

322   which is on the order of the rim distance for some of the starting crystals. Therefore, it can be

323   assumed that if the crystal is homogeneous, the minimum amount of Nb dissolved into the fluid

324   based on the final composition (0.9 wt%) is 11 μg g^{-1}. The maximum amount of Nb dissolved

325   into the fluid if 8 wt% Nb is assumed, is 95 μg g^{-1}.

326   **RESULTS**

14

327   The concentration data for Nb in a 10 wt% NaCl - H_2O fluid, 20 wt% NaCl - H_2O fluid,

328   and 4 wt% NaF - H_2O fluid are provided in Tables 1 (HDAC) and 2 (piston cylinder),

329   respectively. Niobium concentrations in the fluid as a function of: a) temperature; b) pressure;

330   and c) density are presented in Figure 7. Lines in Figure 7 are to provide qualitative insight to the

331   general trends of the data and are not statistical best fits.

332   Niobium concentrations in 10 wt% NaCl-bearing aqueous fluid at 2.1-2.8 GPa range

333   from 6 μg g^{-1} at 300 °C to 11 μg g^{-1} at 500 °C (Table 1; Figure 7), and at 1 GPa from 11-95 μg g^{-1}

334   (minimum to maximum calculated owing to Nb-enriched rims) at 700 °C, to 80-600 μg g^{-1}

335   (minimum to maximum) at 800 °C (Table 2; Figure 7a). The data indicate a positive temperature

336   dependence for the concentration of Nb in the 10 wt% NaCl-bearing aqueous fluid, and a

337   negative pressure and density dependence (Figure 7). The concentration of Nb in a 20 wt%

338   NaCl-bearing aqueous fluid over the temperature range of 300 to 600 °C varies from 55 to 150

339   μg g^{-1}, which is an increase of 2 to 3 times that of the 10 wt% NaCl-bearing fluid. There is no

340   apparent temperature, pressure, or density dependence observed for the 20 wt% NaCl-bearing

341   aqueous fluid. Visual observation of the sample chamber for the experiments with 20 wt% NaCl-

342   bearing fluid indicated that only fluid and Nb-rutile were present; i.e., no salt crystal was

343   observed that could have modified the salinity of the fluid phase. The Nb concentration of the 4

344   wt% NaF-bearing fluid ranges from 180 μg g^{-1} to 980 μg g^{-1} from 300 °C and 2.13 GPa to 500

345   °C and 3.07 GPa, and is 220-1715 μgg^{-1} (minimum to maximum) at 700 °C and 1 GPa. Thus, the

346   addition of NaF to the aqueous fluid increases the concentration of Nb in the fluid by 1 to 2

347   orders of magnitude relative to the addition of NaCl. The concentration of Nb in the 4 wt% NaF-

348   bearing fluid exhibits a positive temperature dependence between 300 and 500 °C at >2 GPa, and

349   no pressure or density dependence. Overall, the new data presented here indicate that the

15

350   concentration of Nb and rutile solubility in saline fluids is strongly dependent on the nature and

351   concentration of the predominant anion (i.e., Cl vs. F) of the fluid.

352   **DISCUSSION**

353   In Figure 7, the experimentally determined Nb concentrations of rutile-saturated aqueous

354   fluids from two published studies are plotted with data from the current study for comparison.

355   Stalder et al. (1998) equilibrated a solid assemblage of clinopyroxene and rutile with pure H_2O at

356   5 GPa and 1000 °C; the clinopyroxene:rutile ratio was 9:1 and 1:1 in the two experiments. They

357   reported that the fluid contained 10.9 μg g^{-1} and 37.6 μg g^{-1} in the two assemblages, respectively,

358   and that the value of $D_{Nb}^{rutile/melt}$ decreased from 0.12 to 0.05, respectively. Brenan et al. (1994)

359   equilibrated rutile and aqueous fluid at 1 and 2 GPa and 900 and 1100 °C. The experimental

360   fluids in that study all contained ~3 wt% dissolved SiO_2, and varied from pure SiO_2-bearing H_2O,

361   to 3.6 wt% HCl-bearing H_2O, to 5.8 wt% NaCl-bearing H_2O, and one experiment with ~300 μg

362   g^{-1} dissolved Al. Their data indicate that the concentration of Nb in the fluid phase varies by one

363   order of magnitude, from ~20 to 300 μg g^{-1}, for pure H_2O, and was ~30 μg g^{-1} for a 5.8 wt%

364   NaCl-bearing fluid.

365   The data for pure H_2O from Brenan et al. (1994) and Stalder et al. (1998) indicate that the

366   concentration of Nb in rutile-saturated H_2O exhibits a positive temperature dependence over the

367   range 900 to 1100 °C (Figure 7a). This is consistent with the new data presented here for the

368   concentration of Nb in a 10 wt% NaCl- and 4 wt% NaF-bearing aqueous fluid (Figure 7a). These

369   observations suggest that temperature has a strong effect on (Ti, Nb)-Cl and (Ti, Nb)-F

370   complexes at moderate to high temperature. However, at higher dissolved salt concentrations, the

371   anion abundance dominates over temperature. This is demonstrated by comparing the data for

372   pure H_2O to the data for 10 and 20 wt% NaCl-bearing aqueous fluids. The apparent temperature

16

373   dependence decreases as the salinity of the fluid increases, until there is an absence of, or at best

374   a very weak, temperature dependence for the 20 wt% NaCl-bearing aqueous fluid. The reduced

375   effect of temperature on the concentration of Nb in fluid as the salinity increases from 10 to 20

376   wt% NaCl most likely reflects the effect of salting out, wherein the concentration of a sparingly

377   soluble metal in aqueous fluid is effected by the strong hydration complexes that form between

378   H_2O and dissociated Na^+, Cl^- and associated NaCl, as the ionic strength of the fluid increases.

379   These hydration complexes effectively reduce the amount of free H_2O molecules available to

380   solvate neutral Nb-Cl complexes. The temperature dependence of Nb in 4 wt% NaF-bearing

381   fluid is also not as pronounced as in pure water or 10 wt% NaCl. It is possible that at lower

382   concentrations of dissolved NaF in aqueous fluid, the relative effect of temperature may be

383   stronger than observed in the present study. These observations are consistent with data in

384   published studies of metal dissolution in NaCl-bearing aqueous fluid (e.g., Hanley et al., 2005),

385   as well as studies of SiO_2 and TiO_2 solubility (Ayers and Watson, 1993; Manning and Boettcher,

386   1994), which have determined experimentally that the influence of temperature on mineral

387   solubility was negligible compared to the effects of fluid composition (Knauss et al., 2001; Rapp

388   et al., 2010; and Wu and Konga, 2013).

389   The data from Brenan et al. (1994) for the concentration of Nb in pure H_2O also indicate

390   that the concentration of Nb in the fluid decreases with pressure (Figure 7b) and density (Figure

391   7c). This is consistent with the results presented here for the concentration of Nb in 10 wt%

392   NaCl-bearing aqueous fluid. This suggests that the stability of the (Ti, Nb)-Cl complex(es) in the

393   fluid decreases with pressure – either in total or by replacement of the dominant complex at low

394   pressure by a different complex at high pressure, which does not complex with Ti or Nb as

395   strongly. The data for 4 wt% NaF- and 20wt% NaCl -bearing fluids do not exhibit any pressure

17

396   dependence. This can be rationalized as a pressure-invariant stability of (Ti, Nb)-halogen

397   complexes. However, it does also imply that these complexes may be different than those

398   dominant in the 10 wt% NaCl -bearing fluid, or that the strong hydration complexes between

399   H_2O and halogens effectively reduce the ability of the fluid to solvate neutral Nb-halogen

400   complexes at higher halogen concentrations. The absence of a temperature dependence of Nb-

401   solubility for the 20 wt% NaCl-bearing fluid and the weak dependence of the solubility on the 4

402   wt% NaF-bearing fluid are consistent with this. The new experimental data presented here

403   demonstrate that at temperatures of 300 to 800 °C and pressures ≥1 GPa, the addition of NaCl

404   and NaF to rutile-saturated aqueous fluid increases the concentration of Nb in the fluid to values

405   higher than predicted from down-temperature extrapolations of experimental data for pure H_2O

406   (Figure 7a). These new results for Nb are consistent with Rapp et al. (2010), who reported that

407   the solubility of pure rutile in aqueous fluid, at 800-1000 °C and 0.5 GPa, increased by

408   approximately two orders of magnitude in aqueous fluid that contained 10 wt% NaCl and 10

409   wt% NaF, relative to pure H_2O. The new data suggest that Ti and Nb are complexed as (Ti, Nb)-

410   chloride and (Ti, Nb)-fluoride in the NaCl-bearing and NaF-bearing experimental fluids,

411   respectively. The determination that NaF enhances the solubility of rutile in aqueous fluid is

412   consistent with predictions based on hard acid – soft base (HASB) considerations (Pearson,

413   1963), and observations from natural systems that Ti and Nb are hydrothermally transported

414   during the evolution of ore deposits associated with alkaline magmatic systems (e.g.,

415   carbonatites; Singer, 1986; Verplanck and Van Gosen, 2011).

416   Timofeev et al. (2014) measured experimentally the solubility of Nb-oxide in F-bearing

417   aqueous fluids at temperatures of 150 to 250 °C and saturated water vapor pressure (SWVP). The

418   activity of fluoride (a(F)) and pH were varied from ~10^5 to 10^{-2} mF and 2.1 to 2.4, respectively.

18

419   They reported that at low a(F), the concentration of Nb in the fluid was pH dependent,

420   interpreted to indicate that Nb-fluoride complexes are present in the fluid. The concentration of

421   Nb in the fluid increased with increasing a(F), independent of pH, which was interpreted to

422   indicate that Nb in the fluid was present as a hydroxyfluoride complex. The relative strength of

423   Nb-halide complexes was assessed computationally by Siegbahn (1993) who performed ab initio

424   calculations to constrain the binding energies of Nb-halide complexes. Siegbahn (1993) reported

425   that the binding energy of Nb-F (135 kcal/mol; bond distance of 1.97 Å) is greater than Nb-Cl

426   (101 kcal/mol; bond distance of 2.46 Å), which is consistent with the measured increase of Nb in

427   the F-bearing aqueous fluid relative to the Cl-bearing aqueous fluid in the present study. In

428   general, binding energies for metal-halide complexes increase in the order Y > Zr > Nb > Mo >

429   Tc > Ru > Rh > Pd, which is also consistent with findings for the strongly enhanced

430   concentration of Y in Cl-bearing aqueous fluids at pressure-temperature conditions similar to

431   those in the present study (Tanis et al., 2012). Siegbahn (1993) found that the increased strength

432   of Nb-F relative to Nb-Cl is related to the interaction between the $4d_\pi$ orbital and the lone pairs of

433   halides, which yields a symmetry that is conducive to attraction by electron donation. The

434   consistency among experimental data sets reported by Timofeev et al. (2014) and Rapp et al.

435   (2010), as well as the ab initio results reported by Siegbahn (1993), with the new data presented

436   in this study, seems to convincingly demonstrate that Nb is fluid-mobile as a Nb-halide complex

437   in saline aqueous fluids.

438   **IMPLICATIONS**

439   The new data presented in this study have implications for the mobility of HFSE in

440   aqueous fluids evolved during prograde metamorphic dehydration reactions that occur during

441   subduction. Brouwer et al. (2012) reported an order of magnitude variation in the concentration

442 of Nb in eclogites from the Franciscan Complex (California) and the Monviso Complex

443 (Western Alps Lago Superiore region). These exhumed terranes equilibrated at a pressure of 1.05

444 GPa and 600 and 500 °C, respectively. Brouwer et al. (2012) invoked the composition of the

445 fluid and degree of fluid-rock interaction as the cause of the order-of-magnitude variation in

446 measured Nb concentrations of the residual rock. The new data presented here indicate that

447 moderately saline aqueous fluid could affect the variability observed in the Franciscan and

448 Monviso Complexes.

449   Spandler et al. (2011) reported that high-pressure veins that cut through eclogite facies

450 (~2 GPa, ~600 °C) Fe-Ti metagabbros in the Monviso Lago Superiore region record subsolidus

451 influx of multiple generations of internally- and externally-derived fluid. The veins contain

452 rutile, garnet, talc and accessory ziron, and the authors reported that rutile grains exhibit zonation

453 of Nb similar to that displayed by other trace elements (e.g., Cr). They also reported extreme Nb

454 enrichment of other minerals such as high-Cr omphacite and garnet, which were assumed to co-

455 precipitate from aqueous fluid. They concluded that the composition of the externally derived

456 fluid responsible for the precipitation of these Cr-rich and Nb-bearing vein minerals (e.g.,

457 omphacite, garnet and rutile) was not only rich in Cr, but also rich in Ni, B, As, Sb and

458 LREE/MREE. The authors noted that Nb might also have been enriched in the fluid phase,

459 although they did not rule out that crystal-chemical effects might dominate Nb incorporation into

460 rutile. Dehydration of serpentitite was invoked as the most plausible source of fluid that would

461 provide multiple episodes of fluid influx and produce the chemistry of the veins (Spandler et al.,

462 2011). Serpentinite dehydration can liberate up to 90% of Cl, more than 80% of B and about

463 50% of Sr from the serpentinite into the fluid, and such fluids can be enriched in Nb, Zr, and

464 LREE (Spandler et al., 2009; Kodolányi and Pettke, 2011). While Nb and other elements such as

20

465   Ti, Zr, Hf, Cr and Ni, are generally regarded as fluid-immobile in subduction zone environments,

466   Spandler et al. (2011) pointed out that the chemical signatures of the veins at Monviso require

467   fluid mobility of Nb and these other elements. Elevated Cl abundances in aqueous fluid would

468   favor scavenging and transport of Nb, as indicated by the data presented in the current study. In

469   fact, high salinity fluid inclusions have been reported for the Monviso gabbros, consistent with

470   the presence of a saline fluid during prograde metamorphism (Barnicoat and Cartwright, 1997;

471   Philippot et al., 1998).

472   Gao et al. (2007) reported the presence of rutile crystals in hydrothermal veins located at

473   the contact between blueschist and eclogite in exhumed rocks in the Tian Shan complex,

474   northwest China. These hydrothermal veins were interpreted by Gao et al. (2007) as evidence for

475   local (i.e., cm to m) transport of HFSE in aqueous fluid evolved during prograde metamorphic

476   dehydration. The eclogite records conditions of ~1.9 GPa and 500 to 600 °C, and the vein records

477   conditions of 1.9 GPa and 490 to 580 °C. These authors reported the presence of aqueous fluid

478   inclusions with salinities of 1.57 to 4.49 wt% NaCl equivalent, and concluded that Nb, Ti and Ta

479   were scavenged by an aqueous fluid during the dehydration of blueschist to eclogite. The new

480   experimental data presented here indicate that Nb would be mobile in a fluid of this composition.

481   Gao et al. (2007) reported that fluid evolution and migration fractionated Nb, Ti and Ta from Zr

482   and Hf, which were sequestered by titanite. Gao et al. (2007) reported that rutile and apatite co-

483   precipitated in the hydrothermal veins. Precipitation of Cl- and F-bearing apatite would result in

484   rapid depletion of these halogens in the fluid, resulting in destabilization of HFSE-fluorine

485   and/or HFSE-chlorine complexes in the fluid. In turn, this would result in precipitation of rutile,

486   which would sequester Nb and other HFSE from the fluid.

487   The sum of observations from natural and experimental systems demonstrate that HFSE

21

488   are mobile in aqueous fluid, and that hydrothermal transport is a function of fluid composition,

489   temperature, and for fluids with ≤10 wt% NaCl equivalent, also dependent on pressure and fluid

490   density. Even in assemblages where rutile is a stable residual phase during prograde fluid

491   evolution, effective mass transfer of Nb to the fluid phase can occur. This was demonstrated by

492   Kessel et al. (2005) who equilibrated aqueous fluid and basaltic eclogite at 4 and 6 GPa and 700

493   to 1200 °C, and reported that $D_{Nb}^{fluid/solid}$ varies by less than a factor of about 5 between rutile-

494   absent and rutile-present assemblages. Kessel et al. (2005) reported that the key parameter, at a

495   given pressure, influencing the fluid mobility of the HFSE in aqueous subcritical fluids, melts

496   and supercritical liquids is temperature. The new data reported here suggest that the findings of

497   Kessel et al. (2005) could represent conservative behavior, and that by adding F and Cl to the

498   aqueous fluid, the mobility of Nb (and thus most of, if not all HFSE) is increased (Figure 7),

499   consistent with observations from exhumed terranes.

500

22

ACKNOWLEDGEMENTS

513   **REFERENCES**

514   Abramson, E.H., and Brown, J.M. (2004) Equation of state of water based on speeds of sound

515   measured in the diamond-anvil cell. Geochimica et Cosmochimica Acta, 68, 1827–1835.

516   Antignano, A., and Manning, C.E. (2008) Rutile solubility in H_2O, H_2O–SiO_2, and H_2O–

517          $NaAlSi_3O_8$ fluids at 0.7–2.0 GPa and 700–1000 °C: Implications for mobility of nominally

518   insoluble element. Chemical Geology, 255, 283-293.

519   Audétat, A., and Keppler, H. (2005) Solubility of rutile in subduction zone fluids, as determined

520   by experiments in the hydrothermal diamond anvil cell. Earth and Planetary Science Letters,

521   232, 393-402.

522   Barnicoat, A.C., and Cartwright, I. (1997) The gabbro-eclogite transformation: an oxygen

23

523   isotope and petrographic study of west Alpine ophiolites. Journal of Metamorphic Geology,

524   15, 93-104.

525 Bassett, W.A., Shen, A.H., Bucknum, M., and Chou, I.-M. (1993) A new diamond anvil cell for

526   hydrothermal studies to 2.5 GPa and from 190 to 1200 °C. Reviews of Scientific Instruments,

527   64, 2340-2345.

528 Bebout, G.E., Ryan, J.G., Leeman, W.P., and Bebout, A.E. (1999) Fractionation of trace

529   elements by subduction zone metamorphism- effect of convergent- margin thermal evolution.

530   Earth and Planetary Science Letters, 171, 63-81.

531 Bose, K., and Ganguly, J. (1995) Experimental and theoretical studies of the stabilities of talc,

532   antigorite and phase A at high pressures with applications to subduction processes. Earth and

533   Planetary Science Letters, 136, 109.

534 Brenan, J.M., Shaw, H.F., Phinney, D.L., and Ryerson, F.J. (1994) Rutile-aqueous fluid

535   partitioning of Nb, Ta, Hf, Zr, U and Th: implications for high field strength element

536   depletions in island-arc basalts. Earth ad Planetary Science Letters, 128, 327-339.

537 Brophy, J.G., and Marsh, B.D. (1986) On the Origin of High-Alumina Arc Basalt and the

538   Mechanics of Melt Extraction. Journal of Petrology, 27, 763-789.

539 Brouwer, F.J., Sorensen, S.S., and Philippot, P. (2012) Physical and chemical evolution of

540   subduction-related eclogites: Interplay of inheritance, alteration, deformation and

541   metamorphism. AGU fall meeting abstract, V43C-2861.

542 Burnley, P.C., and Getting I.C. (2012) Creating a high temperature environment at high pressure

543   in a gas piston cylinder apparatus. Review of Scientific Instruments, 83, 014501.

544 Dorogokupets, P.I., and Dewaele, A. (2007) Equation of state of MgO, Au, Pt, NaCl-B1 and

545   NaCl-B2: Internally consistent high-temperature pressure scales. High Pressure Research, 27,

24

546   431-446.

547   Foley, S.F., Barth, M.G., and Jenner, G.A. (2000) Rutile/melt partition coefficients for trace

548   elements and an assessment of the influence of rutile on the trace element characteristics of

549   subduction zone magmas. Geochimica et Cosmochimica Acta, 64, 933-938.

550   Gao, J., John, T., Klemd, R., and Xiong, X. (2007) Mobilization of Ti–Nb–Ta during subduction:

551   Evidence from rutile-bearing dehydration segregations and veins hosted in eclogite,

552   Tianshan, NW China. Geochimica et Cosmochimica Acta, 71, 4974-4996.

553   Gill J.B. (1981) Orogenic Andesites and Plate Tectonics. Springer- Verlag, 390.

554   Green T.H. (1981) Experimental evidence for the role of accessory phases in magma genesis.

555   Journal of Volcanology and Geothermal Research, 10, 405-422.

556   Hacker, B.R. (2008) H_2O subduction beyond arcs. Geochemistry Geophysics Geosystems, 9, 1-

557   24.

558   Hammersley, A.P. (1997) FIT2D: An Introduction and Overview. ESRF Internal Report,

559   ESRF97HA02T.

560   Hanchar, J.M., Finch, R.J., Hoskin, P.W.O, Watson, E.B., Cherniak, D.J., and Mariano, A.N.

561   (2001) Rare earth elements in synthetic zircon: Part 1. Synthesis, and rare earth element and

562   phosphorus doping. American Mineralogist, 86, 667-680.

563   Hanley, J.J., Pettke, T., Mungall, J.E., and Spooner, E.T.C. (2005) The solubility of platinum and

564   gold in NaCl brines at 1.5 kbar, 600 to 800 °C: A laser ablation ICP-MS pilot study of

565   synthetic fluid inclusions. Geochimica et Cosmochimica Acta, 69, 2593-611.

566   Hawkesworth, C.J., Hergt, J.M., Ellam, R.M., and McDermott, F. (1991) Element fluxes

567   associated with subduction related magmatism. Philosophical Transactions of the Royal

568   Society of London, 335, 393–405.

569   Hawkesworth, C.J., Gallagher, K., Hergt, J.M., and McDermott, F. (1993a) Mantle and slab

570   contributions in arc magmas. Annual Review of Earth and Planetary Sciences, 21, 175-204.

571   Hawkesworth, C.J. (1993b) Trace Element Fractionation Processes in the Generation of Island

572   Arc Basalts. Philosophical Transactions of the Royal Society of London, Series A, 342, 179-

573   191.

574   Hayden, L.A., and Manning, C.E. (2011) Rutile solubility in supercritical $NaAlSi_3O_8$-H_2O fluids.

575   Chemical Geology, 284, 74-81.

576   Hernlund, J., Leinenweber, K., Locke, D., and Tyburczy, J.A. (2006) A numerical model for

577   steady-state temperature distributions in solid-medium high-pressure cell assemblies.

578   American Mineralogist, 91, 295-305.

579   Jenner, G.A., Foley, S.F., Jackson, S.E., Green, T.H., Fryer, B.J., and Longerich, H.P. (1994)

580   Determination of partition coefficients for trace elements in high pressure-temperature

581   experimental run products by laser ablation microprobe-inductively coupled plasma-mass

582   spectrometry (LAM-ICP-MS). Geochemica et Cosmochimica Acta, 58, 5099-5103.

583   Kelemen, P.B., Johnson, K.T.M., Kinzler, R.J., and Irving, A.J. (1990) High-field-strength

584   element depletions in arc basalts due to mantle–magma interaction. Nature, 345, 521-524.

585   Kerrigan, R.J. (2011) Reaction Rates and textural development of hydrolysis reactions in the

586   system MgO-SiO_2-H_2O. Dissertation, University of Maryland.

587   Kessel, R., Schmidt, M.W., Ulmer, P., and Pettke, T. (2005) Trace element signature of

588   subduction-zone fluids, melts and supercritical liquids at 120-180 km depth. Nature 437,

589   724-727.

590   Kodolányi, J., and Pettke, T. (2011) Loss of trace elements from serpentinites during fluid-

591   assisted transformation of chrysotile to antigorite -An example from Guatemala. Chemical

26

592   Geology, 284, 351-362.

593   Manning, C.E., Wilke, M., Schmidt, C., and Cauzid, J. (2008) Rutile solubility in albite-H_2O and

594       $Na_2Si_3O_7$-H_2O at high temperatures and pressures by in-situ synchrotron radiation micro-

595   XRF. Earth and Planetary Science Letters, 272, 730-737.

596   Manning, C.E. (2004) The chemistry of subduction-zone fluids. Earth and Planetary Science

597   Letters, 223, 1-16.

598   Manning, C.E., and Boettcher, S.L. (1994) Rapid-quench hydrothermal experiments at mantle

599   pressures and temperatures. American Mineralogist, 79, 1153-1158.

600   Mantegazzi, E., Sanchez-Valle, C., and Driesner, T. (2013) Thermodynamic properties of

601   aqueous NaCl solutions to 1073 K and 4.5 GPa, and implications for dehydration reactions in

602   subducting slabs. Geochimica et Cosmochimica Acta, 121, 263-290.

603   Marschall, H.R., Dohmen, R., and Ludwig, T. (2013) Diffusion-induced fractionation of niobium

604   and tantalum during continental crust formation. Earth and Planetary Science Letters, 375,

605   361-371.

606   McCulloch, M.T., and Gamble, J.A. (1991) Geochemical and geodynamical constraints on

607   subduction zone magmatism. Earth and Planetary Science Letters, 102, 358-374.

608   Pearson, R.G. (1963) Hard and soft acids and bases. Journal of the American chemical society,

609   85, 3533-3539.

610   Pettke, T. (2006) In situ laser-ablation-ICP-MS chemical analysis of melt inclusion and prospects

611   for constraining subduction zone magmatism. Mineralogical Association of Canada Short

612   Course, 36, 51-80.

613   Pettke, T., Oberli, F., Audétat, A., Guillong, M., Simon, A.C., Hanley, J.J., and Klemm, L.M.

614   (2012) Recent developments in element concentration and isotope ratio analysis of individual

27

615   fluid inclusions by laser ablation single and multiple collector ICP-MS. Ore Geology

616   Reviews, 44, 10-38.

617   Philippot, P., Agrinier, P., and Scambelluri, M. (1998) Chlorine cycling during subduction of

618   altered oceanic crust. Earth and Planetary Science Letters, 161, 33-44.

619   Rapp, J.R., Klemme, S., Butler, I.B., and Harley, S.L. (2010) Extremely high solubility of rutile

620   in chloride and fluoride-bearing metamorphic fluids: An experimental investigation.

621   Geology, 38, 323.

622   Ryerson, F.J., and Watson, E.B. (1987) Rutile saturation in magmas: implications for Ti Nb Ta

623   depletion in island-arc basalts. Earth and Planetary Science Letters, 86, 225-239.

624   Sanchez-Valle, C., Martinez, I., Daniel, I., Philippot, P., Bohic, S., and Simionovici, A. (2003)

625   Dissolution of strontianite at high P-T conditions: An in situ synchrotron X-ray fluorescence

626   study. American Mineralogist, 88, 978–985.

627   Saunders A.D., Tarney J., and Weaver S.D. (1980) Transverse geochemical variations across the

628   Antarctic Peninsula: implications for the genesis of calc-alkaline magmas. Earth and

629   Planetary Science Letters, 46, 344–360.

630   Schmidt, C., Rickers, K., Bilderback, D.H., and Huang, R. (2007) In situ synchrotron radiation

631   XRF study of REE phosphate dissolution in aqueous fluids to 800 °C. Lithos, 95, 87-102.

632   Sheppard, L.R., Atanacio, A.J., Bak, T., Nowotny, J., and Prince, K.E. (2007) Bulk diffusion of

633   niobium in single-crystal titanium dioxide. Journal of Physical Chemistry B, 111, 8126-8130.

634   Siegbahn, P.E.M. (1993) A comparative study of the bond strengths of the second row transition

635   metal hydrides, fluorides, and chlorides. Theoretica Chimica Acta, 86, 219-228.

636   Singer, D.A. (1986) Grade and tonnage model of carbonatite deposits. *In* Cox, D.P. and Singerl,

637   D.A., eds., Mineral deposit models. United States Geologial Survey Bulletin, 1693, 51.

28

638   Spandler, C., Pettke, T., and Hermann, J. (2009) The composition of serpentinite dehydration

639   fluids in subduction zones: an experimental study. Geochimica et Cosmochimica Acta, 73,

640   Supplement 1, A1256.

641   Spandler, C., Pettke, T., and Rubatto, D. (2011) Internal and External Fluid Sources for Eclogite-

642   facies Veins in the Monviso Meta-ophiolite, Western Alps: Implications for Fluid Flow in

643   Subduction Zones. Journal of Petrology 52, 1207-1236.

644   Stalder, R., Foley, S.F., Brey, G.P., and Horn, I. (1998) Mineral-aqueous fluid partitioning of

645   trace elements at 900-1200 °C and 3.0-5.7 GPa: New experimental data for garnet,

646   clinopyroxene, and rutile, and implications for mantle metasomatism. Geochimica et

647   Cosmochimica Acta, 62, 1781-1801.

648   Tanis, E.A., Simon, A.C., Tschauner, O., Chow, P., Xiao, Y., Shen, G., Hanchar, J.M., and

649   Frank, M. (2012) Solubility of xenotime in a 2 M HCl aqueous fluid from 1.2 to 2.6 GPa and

650   300 to 500 °C. American Mineralogist, 97, 1708–1713.

651   Timofeev, A., Migdisov, A.A., and Williams-Jones, A.E. (2014) The solubility and speciation of

652   niobium in fluoride-bearing aqueous solutions. Goldschmidt Conference.

653   Tropper, P., and Manning, C.E. (2005) Very low solubility of rutile in H_2O at high pressure and

654   temperature, and its implications for Ti mobility in subduction zones. American

655   Mineralogist, 90, 502-50.

656   Verplanck, P.L., and Van Gosen, B.S. (2011) Carbonatite and alkaline intrusion-related rare

657   earth element deposits – A deposit model. United States Geological Survey Open File

658   Report, 1256.

659   Wojdyr, M. (2010) Fityk: a general-purpose peak fitting program. Journal of Applied

660   Crystallography, 43, 1126–1128.

29

661   Woodhead, J., Eggins, S., and Gamble, J. (1993) High field strength and transition element

662   systematics in island arc and back-arc basin basalts: evidences for multi-phase melt

663   extraction and a depleted mantle wedge. Earth and Planetary Science Letters, 114, 491-504.

664

665   FIGURE CAPTIONS

666   **Figure 1**. The experimental P-T conditions for the current study are plotted with respect to

667   subduction paths for cold and hot subduction (cf. Hacker et al., 2008). The P-T conditions for

668   published experimental data for the solubility of pure rutile in pure H_2O (circles, Tropper and

669   Manning, 2005; Audétat and Keppler, 2005; Antignano and Manning 2008; Rapp et al., 2010),

670   NaCl-aqueous fluids (triangles, Rapp et al., 2010) and NaF-aqueous fluids (diamonds, Rapp et

671   al., 2010). The P-T conditions for studies of Nb partitioning between rutile and aqueous fluid and

672   silicate melt are also plotted (pentagons; Brenan et al., 1994, Stalder et al., 1998, Foley et al.,

673   2000).

674

675   **Figure 2.** EPMA-determined Nb (squares) and Mo (triangles) concentrations (wt%) of polished,

676   randomly selected starting crystals as a function of distance from the rim towards the center of

677   the crystal (a, b), and LA-ICP-MS depth profiles into the crystals perpendicular to the growth

678   surface (c, d). The error is within the size of the symbol.

679

680   **Figure 3.** The LA-ICP-MS depth profiles of ^{49}Ti (blue circles) and ^{93}Nb (red squares)

681   concentrations in the (a) starting crystal and (b) run-product crystal from the piston cylinder-

682   mass loss experiment 20130314. Gas background is measured for the first 30-40 seconds at

683   which time the laser is turned on and used to ablate the crystal. The elevated Nb signal duration

684   in (a) corresponds to several μm thickness ablated at the LA-ICP-MS conditions employed.

685

686   **Figure 4.** The normalized experimental spectra of the 1000 μg g^{-1} Nb standard.

31

687

688   **Figure 5.** The Nb standard calibration. The normalized integrated peak area of SXRF spectra

689   from the 300 and 1000 μg g^{-1} Nb standard plotted against concentration to demonstrate linearity

690   of the calibration.

691

692   Figure 6. The integrated, unnormalized, raw data as a function of time for Runs 20110804 (top)

693   and 20110805 (bottom) are shown. Experimental data that contained an average standard

694   deviation over the entire time range of less then 15% were used in further analysis. A fit of the

695   data was made to ensure that the R^2 value was <0.1, essentially time invariant. During Run

696   20110804, at 300 °C there were large variations (average standard deviation >12%) in the signal,

697   due to major beam fluctuations, therefore only 300°C data in the later time frame (where R^2 of

698   the fit <0.02) was used.

699

700   SXRF maps of the sample chamber. a) (top left) and b) (top right) 2-D and 3-D, respectively,

701   false-color maps of x-ray beam intensity that passed through sample chamber. c) (bottom left)

702   and d) (bottom right) 2-D and 3-D false-color maps, respectively, of the Nb signal intensity from

703   the sample chamber. The color bar is based on beam (for a and b) or Nb intensity (for c and d).

704   Red colors are high intensity and purple colors are low intensity. The scale is divided into 4000

705   count increments for beam intensity and 10 count increments for Nb intensity.

706

707   **Figure 7.** Nb concentrations in experimental aqueous fluids plotted as a function of (a)

708   temperature, (b) pressure, and (c) fluid density. Also plotted are published data from Brenan et

709   al., (1994) and Stalder et al., (1998). Uncertainties for Nb (μg g^{-1}) are discussed in the text. The

32

710   bars without symbols represent the piston cylinder data (1 GPa, 700 and 800 °C) minimum and

711   maximum Nb concentrations as described in the text.

712

713   Table 1: HDAC-SXRF experimental conditions and results

Experiment[a]	Fluid Type (wt%)	Temperature (°C)	Pressure (GPa) ($\pm 1\sigma$)	Fluid Density (g/cm^3)	μg g^{-1} Nb in the fluid ($\pm 1\sigma$)[b,c]
20110801	10% NaCl	300	2.10(0.1)	1.25	6(1)
20110801	10% NaCl	400	2.80(0.1)	1.28	8(1)
20110801	10% NaCl	500	2.80(0.1)	1.25	11(2)
20110804	20% NaCl	300	2.05(0.1)	1.38	140(20)
20110804	20% NaCl	400	2.62(0.1)	1.41	150(20)
20110804	20% NaCl	500	4.56(0.2)	1.54	150(20)
20110804	20% NaCl	600	6.36(0.2)	1.63	140(20)
20110805	20% NaCl	300	1.80(0.1)	1.21	75(7)
20110805	20% NaCl	400	2.60(0.1)	1.27	65(7)
20110805	20% NaCl	500	4.50(0.2)	1.38	55(7)
20120802	4% NaF	308	5.14(1.1)	1.50	190(25)
20120802	4% NaF	401	5.19(1.1)	1.49	560(65)
20120802	4% NaF	503	6.53(1.4)	1.54	700(70)
20130202	4% NaF	300	3.21(0.4)	1.39	200(40)
20130202	4% NaF	400	3.48(1.0)	1.37	420(80)
20130205	4% NaF	300	2.13(0.6)	1.29	180(20)
20130205	4% NaF	400	2.48(0.3)	1.30	910(90)
20130205	4% NaF	500	3.07(0.4)	1.32	980(50)

714   [a]Each experimental SXRF run allows us to measure the concentration of Nb in aqueous fluid at
715   multiple P-T conditions. Rutile crystals are not recovered at each unique PT point; thus, partition
716   coefficients are not reported.
717   [b]The reported uncertainty for the SXRF data reflects propagation of error from the standard
718   calibration and peak fitting.
719   [c]Corrected for absorption and density as described in the text.
720

34

721

722 Table 2: Piston cylinder experimental conditions and results

Experiment ID	20130314	20130522	20130527[b]
Fluid Composition (wt%)	10% NaCl	10% NaCl	4% NaF
Time (h)	8:31	27:15	12:00
Temperature ($^{\circ}$C) ($\pm 1\sigma$)	687(2)	793(11)	692(7)
Pressure (GPa) ($\pm 1\sigma$)	1.09(0.06)	1.04(0.02)	0.97(0.02)
Fluid (mg)	23.4	31.2	29.5
Fluid Density (g/cm^3)	1.06	1.01	0.91
[a]Crystal weight in (μg) ($\pm 1\sigma$)	547(12)	887(5)	1088(1)
[a]Crystal weight out (μg) ($\pm 1\sigma$)	523(6)	734(5)	651(162)
Mass loss (μg)	24	153	437
[c]Wt% Nb in product crystal	0.9307(.04)	1.0456(0.06)	1.0275(0.22)
[d]μg g^{-1} Nb in Fluid min ($\pm 1\sigma$)	11(1)	80(5)	220(50)
[e]μg g^{-1} Nb in Fluid max ($\pm 1\sigma$)	95(5)	600(35)	1715(370)

723

724 [a]The crystal was weighed four times and the average mass is reported. The one sigma standard

725 deviation of the average mass is provided in parentheses.

726 [b]Run products contained broken crystal fragments as well as the primary crystals.

727 [c]Wt% Nb for final run products are from LA-ICP-MS analysis.

728 [d]Minimum Nb concentration in the fluid calculated by using the final wt% Nb from LA-ICP-MS.

729 Error is calculated by propagating the error from weighing and the analytical error from the LA-

730 ICP-MS.

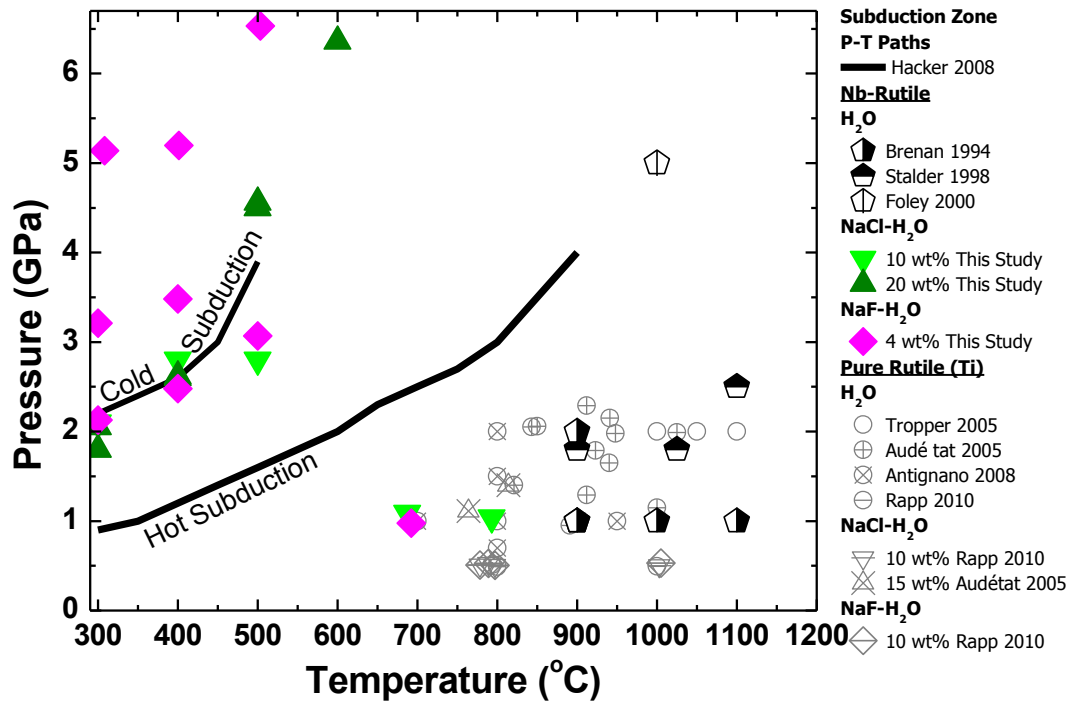731 [e]Maximum Nb concentration in the fluid is calculated by using 8 wt% Nb (see text for

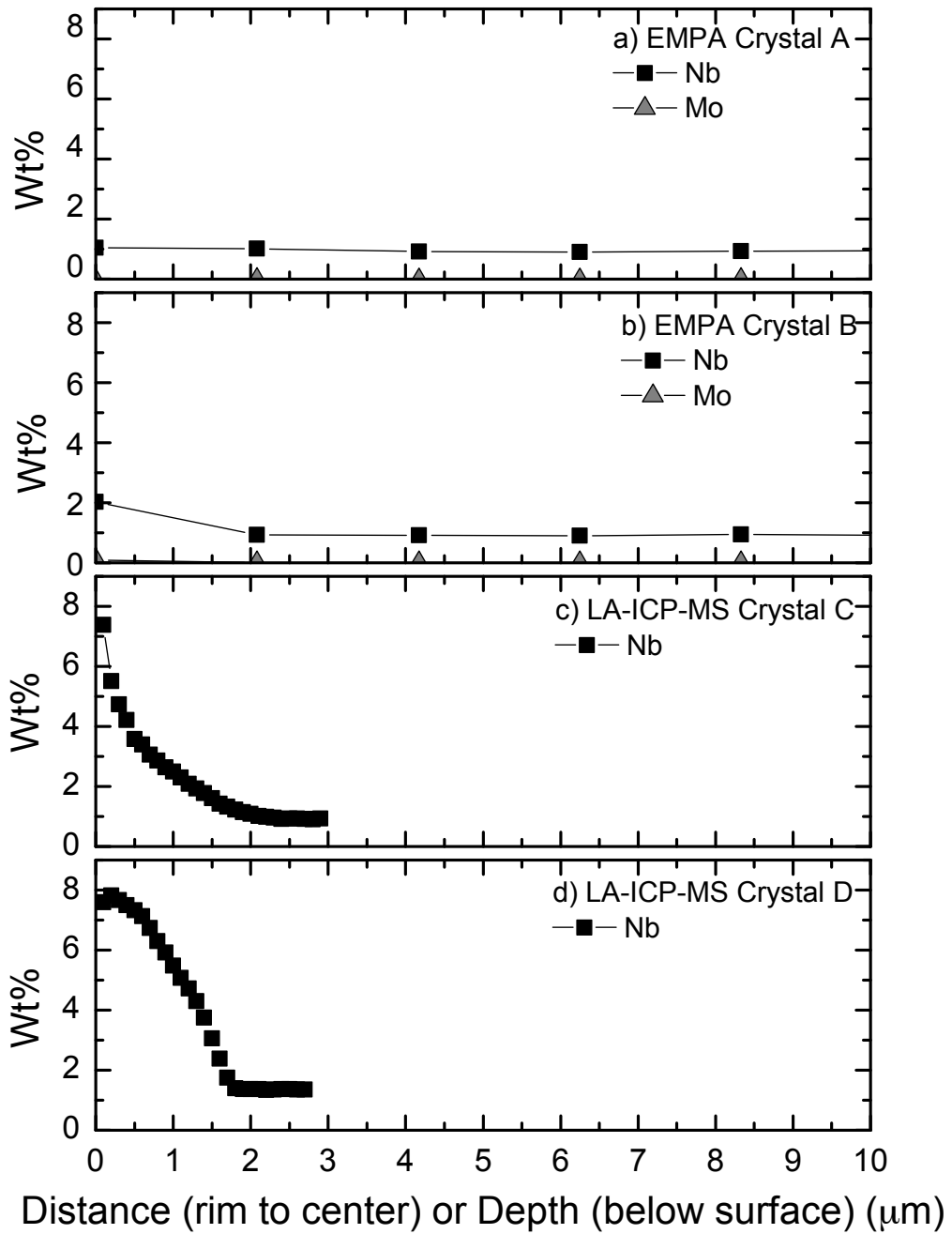732 discussion).

35

733

734   FIGURES
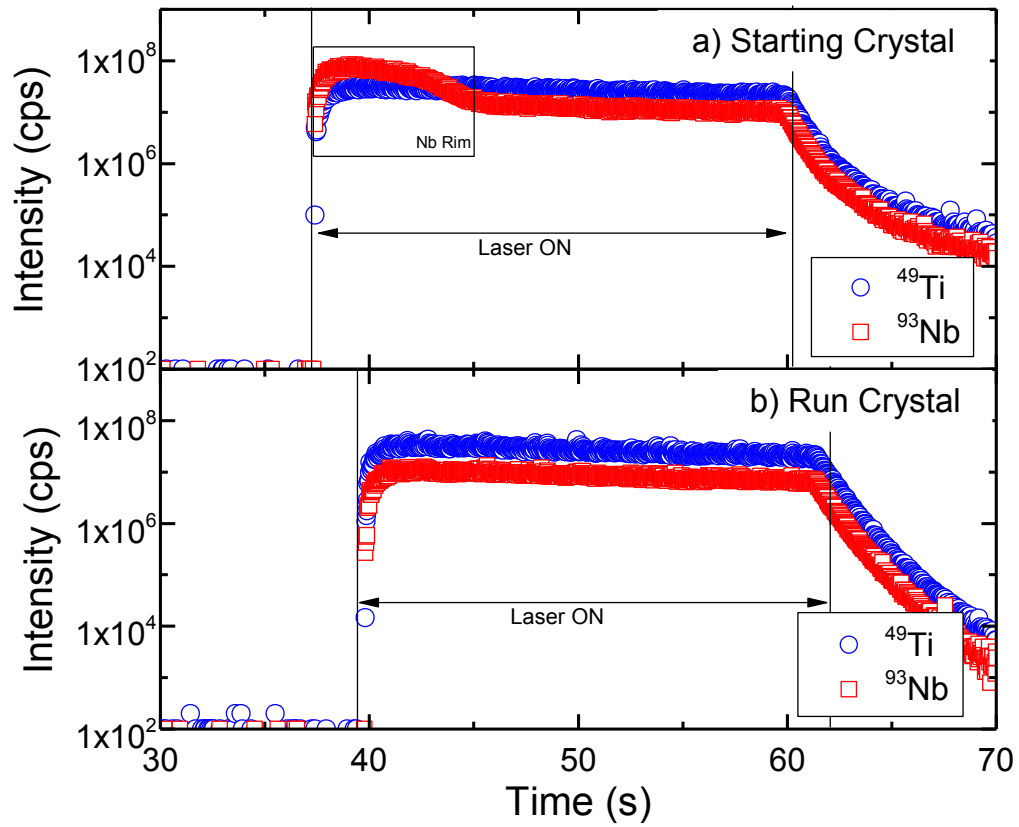
735   Figure 1.

736

737

738   Figure 2

Distance (rim to center) or Depth (below surface) (μm)

739

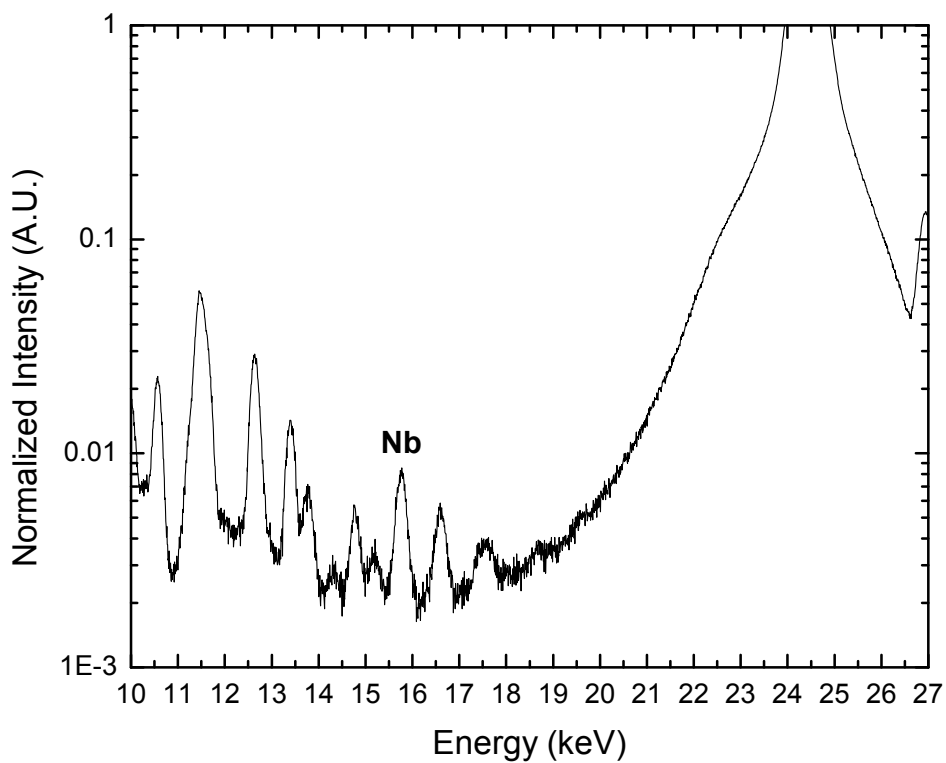740   Figure 3

741

742

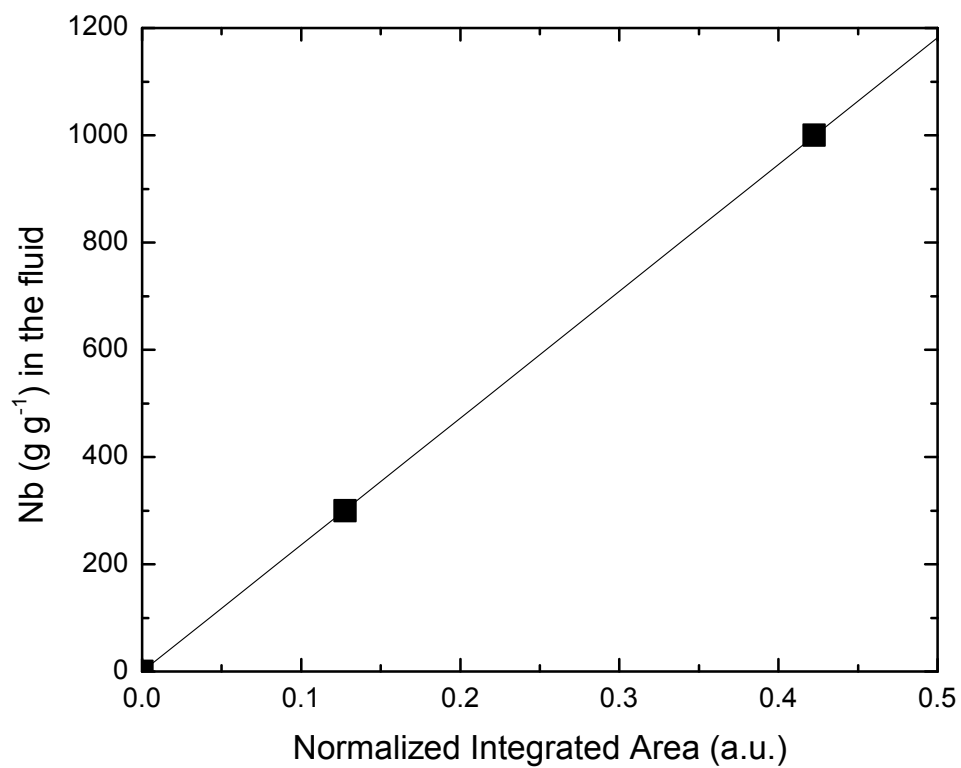743   Figure 4

744

745

746
747   Figure 5:

748

749

750

751

40
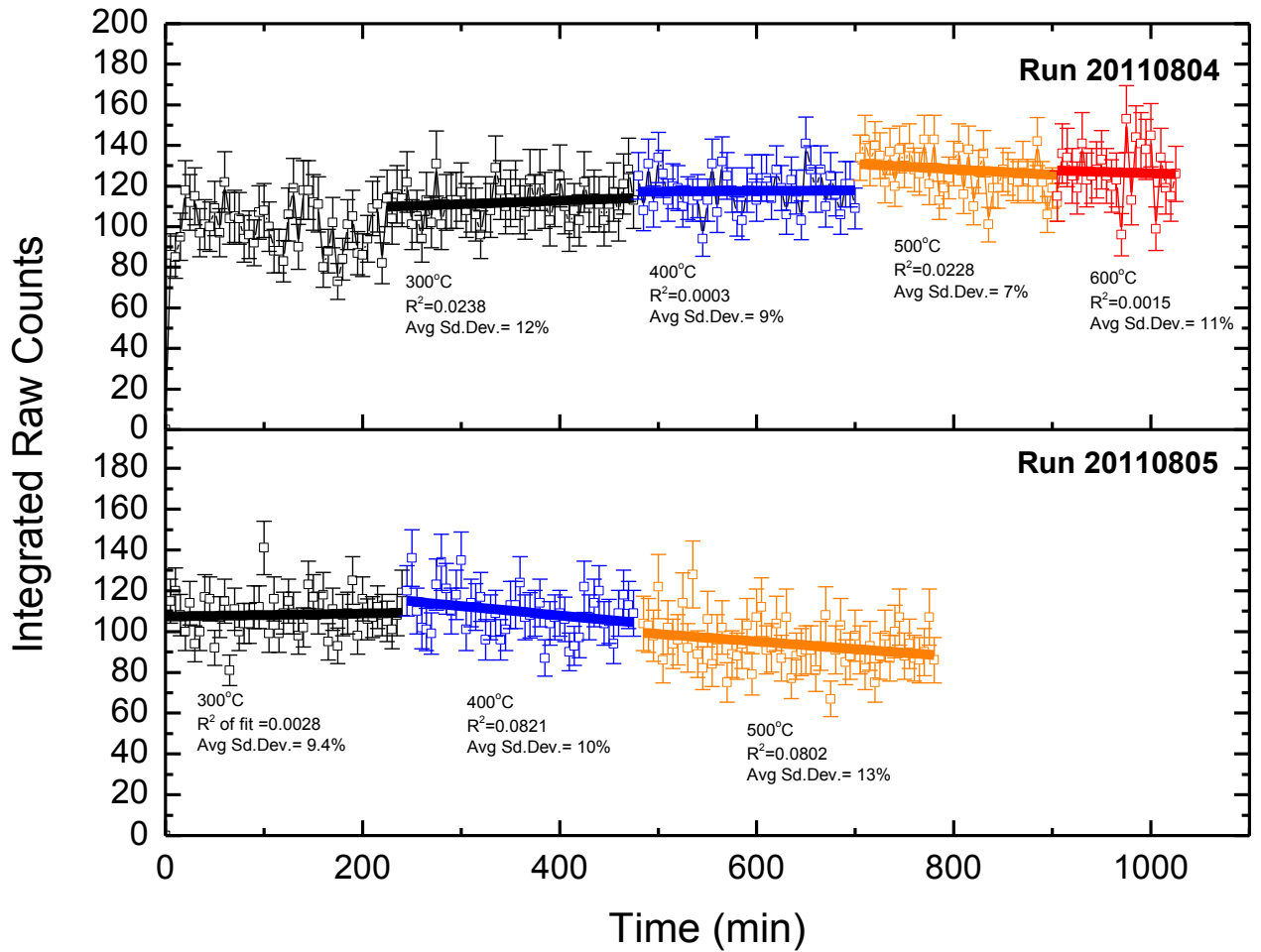
752
753   Figure 6
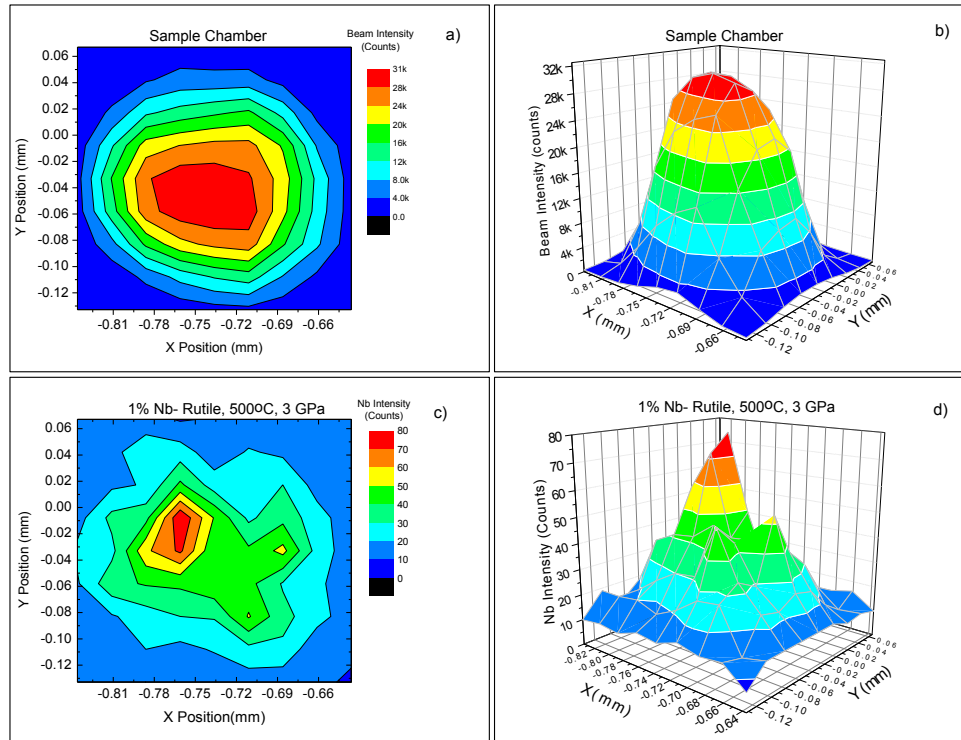
754

755

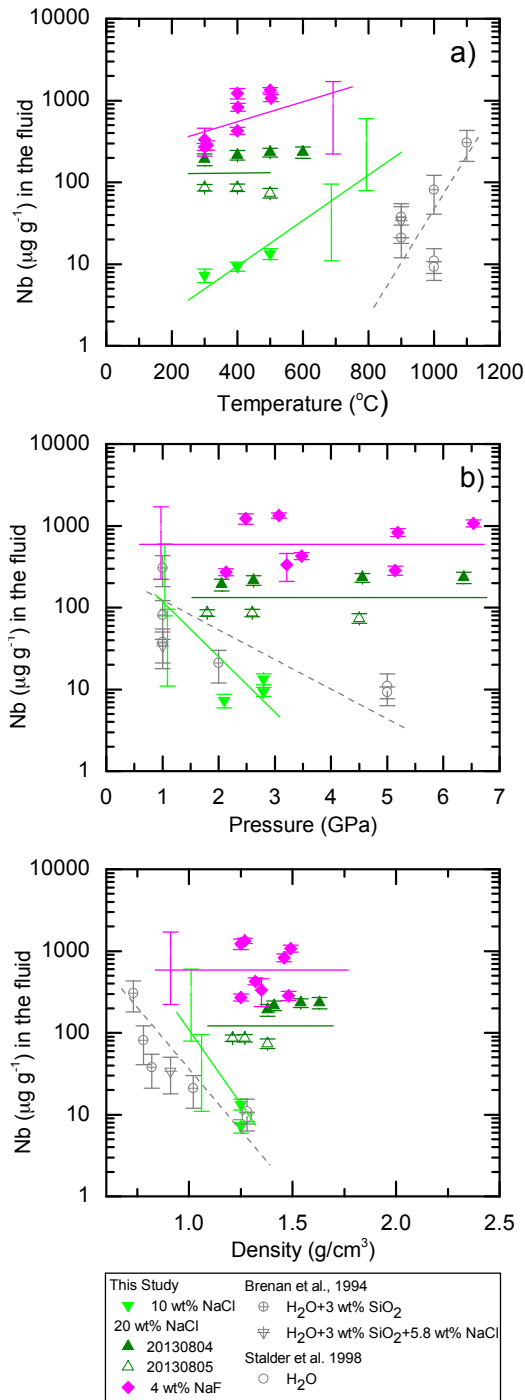756

757   Figure 7

758

759

760

761

762

763

764

765

766

767

42

768

769   Figure 8

770

43